



**Electrocatalytic Water Oxidation Performance in an
Extended Porous Organic Framework with a Covalent
Alliance of Distinct Ru-Sites**

Journal:	<i>Nanoscale</i>
Manuscript ID	NR-ART-03-2022-001297.R1
Article Type:	Paper
Date Submitted by the Author:	25-Apr-2022
Complete List of Authors:	<p>Mondal, John; Indian Institute of Chemical Technology, Inorganic and Physical Chemistry Boro, Bishal ; Indian Institute of Chemical Technology CSIR, Catalysis & Fine Chemicals Adak, Mrinal ; Indian Institute of Technology Delhi, Chemistry Biswas, Sohag; University of California Riverside, Department of Chemical & Environmental Engineering, Materials Science & Engineering Program Sarkar, Chitra; Indian Institute of Chemical Technology, Inorganic & Physical Chemistry Division Nailwal, Yogendra; Indian Institute of Science Education and Research Mohali, Chemical Sciences Shrotri, Abhijit; Hokkaido University, Institute for Catalysis Chakraborty, Biswarup; Indian Institute of Technology Delhi, Chemistry Wong, Bryan; University of California Riverside, Department of Chemical & Environmental Engineering, Materials Science & Engineering Program</p>

Electrocatalytic Water Oxidation Performance in an Extended Porous Organic Framework with a Covalent Alliance of Distinct Ru-Sites†

Bishal Boro,^{a,b} Mrinal K. Adak,^c Sohag Biswas,^d Chitra Sarkar,^{a,b} Yogendra Nailwal,^e Abhijit Shrotri,^f Biswarup Chakraborty,^{*,c} Bryan M. Wong,^{*,d} and John Mondal^{*,a,b}

^aDepartment of Catalysis & Fine Chemicals, CSIR-Indian Institute of Chemical Technology, Uppal Road, Hyderabad-500007, India, Email: johnmondal@iict.res.in; johncuchem@gmail.com

^bAcademy of Scientific and Innovative Research (AcSIR), Ghaziabad- 201002, India.

^cDepartment of Chemistry, Indian Institute of Technology Delhi, Hauz Khas, 110016, New Delhi, India. Email: cbiswarup@chemistry.iitd.ac.in

^dDepartment of Chemical & Environmental Engineering, Materials Science & Engineering Program, Department of Chemistry, and Department of Physics & Astronomy, University of California-Riverside, Riverside, California 92521, United States. Email: bryan.wong@ucr.edu

^eDepartment of Chemical Sciences, Indian Institute of Science Education and Research (IISER) Mohali, Sector 81, Knowledge City, Manauli 140306, India.

^fInstitute for Catalysis, Hokkaido University, Kita 21 Nishi 10, Kita-ku, Sapporo, Hokkaido 001-0021, Japan.

†**Electronic supplementary information (ESI) available:** Materials and methods, characterization techniques, ¹H, ¹³C NMR and ESI-MS spectra of (Ru(demob)₃Cl₂), thermogravimetric analysis (TGA), wide-angle powder X-ray diffraction pattern, FT-IR spectrum, additional TEM, FE-SEM images, X-ray photoelectron spectroscopy (XPS) survey spectrum, cyclic voltammetry analysis, TEM and FE-SEM images of reused catalyst.

Abstract

The rational synthesis of durable, earth-abundant efficient electrocatalysts for the oxygen evolution reaction (OER) from water is one of the most significant routes for storing renewable energy and minimizing fossil fuel combustion. The prime hurdles for effectively utilizing commercial RuO₂ as (OER) electrocatalyst are its very low stability, catalyst deactivation, and high cost. In this work we explored a Ru integrated porous organic polymer (**Ru@Bpy-POP**) by a facile one-pot Friedel-Craft alkylation strategy between redox-active Ru(demob)₃Cl₂ and a carbazole unit, which is comprised of unique features including an extended framework unit, isolated active sites, and tunable electrode kinetics. **Ru@Bpy-POP**

can serve as a bridge between a Metal-Organic Framework (MOF) and POP-based catalytic systems with a balanced combination of covalent bonds (structural stability) and open metal sites (single site catalysis). **Ru@Bpy-POP**, deposited on a three-dimensional nickel foam electrode support, exhibits a promising electrocatalytic OER activity with an ultra-low ruthenium loading compared to a benchmark RuO₂ catalyst, providing an overpotential of about 270 mV to reach 10 mA cm⁻² in an alkaline medium. Moreover, a high current density of 248 mA cm⁻² was achieved for the **Ru@Bpy-POP** catalyst at only 1.6 V (vs. RHE), which is much higher than 91 mA cm⁻² of commercial RuO₂. The robust, albeit highly conjugated POP framework, not only triggered facile electro-kinetics but also suppressed aggregation and metallic corrosion during electrolysis. In particular, the benefits of covalent integration of distinct Ru-sites into the framework can modulate intermediate adsorption and charge density, thereby becoming a prime factor behind the exceptional OER activity. All of the critical steps involved in OER are complemented by Density Functional Theory (DFT) calculations, which suggest that electrocatalytic water oxidation proceeds from a closed-shell configuration to open-shell electronic configurations with high-spin states. These open-shell configurations are more stable than their closed-shell counterparts by 1 eV, improving the overall catalytic activity.

Keywords: *Porous organic polymer (POP), Integrated metalated POP, Electrocatalytic Water Oxidation, distinct Ru-active sites, DFT*

Introduction:

Environmental pollution is closely correlated with non-renewable fossil fuel combustion by the emission of greenhouse gases to the earth's atmosphere during the combustion process. Hence, the discovery of clean and sustainable energy sources to confront the energy crisis and prevent further destruction to the environment has become utterly important. Since the ocean covers 71% of the earth's surface, the utilization of water to produce clean-energy H₂ accompanied by O₂ evolution could provide a vast opportunity to tackle the above-mentioned issues.¹ The water oxidation or oxygen evolution reaction (OER) is the most complex transformation process compared to hydrogen reduction, which is kinetically sluggish and requires a large overpotential.² The equilibrium potential of OER is as high as 1.23V vs. RHE, and most of the materials susceptible towards oxidation produced from this high potential eventually lead to the deterioration of electrode efficiency.³ On the other hand,

relentless bubble release under a high current density introduces a bubble shielding effect and problems related to catalyst peel-off.⁴ As such, the development stable and efficient OER catalyst remains a challenge to this day.

Several homogeneous metal complexes have been developed for electrocatalysis in which freely diffusing catalytically active sites play the lead role in the catalytic transformation process. Although mechanistic insight could be easily gained by relatively more straightforward characterizations of the homogeneous catalytic system, catalyst deactivation during the reaction and sluggish electron transfer from the electrode has made the entire process economically non-viable. However, the heterogeneous catalytic system (which overcomes the issues mentioned above) still suffers from synthetic versatility and a more superficial characterization for mechanistic insight. Hence, using heterogeneous molecular complexes could be an excellent opportunity to maximize its activity severalfold through proper use and modulation of the kinetics of the electron transfer process. Noble metal oxides such as IrO₂ and RuO₂ are widely explored as efficient OER electrocatalysts;⁵ however, the lower abundance and higher cost of these materials hinder their large-scale industrial application. Enormous efforts have resulted in low-cost, stable, and efficient OER catalysts. In addition, Metal-Organic Frameworks (MOFs) have been widely utilized in electronic devices, water-harnessing technologies, and catalysis, because of their well-defined compositions, crystalline structures, and tunable coordination space.⁶⁻⁸

However, MOFs exhibit several problems that include chemical, thermal, and mechanical instability when exposed to various chemical environments (e.g., moisture, solvents, acids, bases, as well as heat, vacuum, or pressure treatment).^{9,10} On the other hand, the unique pores generated through covalent bonding in porous organic polymers (POPs) facilitate electron and mass transfer.¹¹ Moreover, atomically precise structures of the porous framework not only provide stability to the molecular active site but also render immobilization of active species throughout the porous channels during the reaction compared to other heterogeneous support systems. Most importantly, the secondary environment around the catalytically active sites could be efficiently modulated by introducing nodes and linkers into the organic building blocks to generate new electrochemical properties, which are absent in the individual counterparts. Catalytic porous organic polymers are comprised of various metals as node/linkers and utilize redox-active functional building blocks to activate the substrate. Hence, the incorporation of molecular catalysts inside the porous architecture could bridge the gap between homogeneous and heterogeneous catalysts with exceptional electrocatalytic

activity compared to molecular analogs. Thus, the metal site in the POP framework can efficiently manipulate the electronic properties of the active site by promoting the electron transfer process. There are various synthetic approaches available to synthesize metallated POPs, such as coupling the reaction between metallated building blocks and the monomeric unit, post-synthetic metalation of POPs, and successful incorporation of metal NPs or clusters inside the pores of POPs.¹² Recently, Maji and co-workers have developed azo functionalized POPs to coordinate with Co^{II} for efficient water oxidation accompanied by very low metal loading (8%) with an overpotential of 340 mV in alkaline solutions.¹¹ Bimetallic NiFe-based porous organic polymers with a high surface area almost exhibited a similar electrocatalytic activity as RuO₂ at a low overpotential of 338 mV.¹³ These heteroatom-incorporated POPs with active metal sites have enabled an immense opportunity in electrocatalysis.

Emissive transition-metal complex ruthenium-tris(bipyridine), [Ru(bpy)₃]²⁺ has attracted significant attention due to its promising redox and photophysical characteristics.¹⁴ [Ru(bpy)₃]²⁺ derivatives also have versatile applications in the field of optoelectronics, molecular switches, information storage, and the design of sensors.¹⁵⁻¹⁷ In addition, the unique characteristics of the carbazole unit, including a reversible one-electron transfer process has been critically evaluated for redox-active building blocks to design an active electrocatalyst.¹⁸ In this work we utilize a Ru-Metallated POP design strategy with redox-active tris(4,4'-dimethoxy-2,2'-bipyridyl) ruthenium (II) dichloride (**Ru(demob)₃Cl₂**) and a carbazole moiety. We utilize a simple one-step Friedel Crafts reaction to furnish **Ru@Bpy-POP** that combines a good charge carrier mobility and excellent oxidative stability for the OER reaction. **Ru@Bpy-POP** could effectively increase electrocatalytic water oxidation activity with an ultra-low catalyst loading compared to commercial RuO₂ catalysts. All of the critical steps involved in OER are complemented by Density Functional Theory (DFT) calculations to provide mechanistic insight into these reactions.

Experimental Section:

Synthesis of Ru(demob)₃Cl₂(Ru@Bpy): In a typical synthesis procedure, 4,4'-Dimethoxy-2,2'-bipyridine (1.5 mmol, 324 mg) in EtOH (15 ml) was charged into an oven-dried two-neck round bottom flask and stirred for 5 mins at N₂ atmosphere. The metal precursor RuCl₃·xH₂O (0.5 mmol, 104 mg) was then dissolved in 5 ml EtOH and added dropwise to the former reaction mixture with the help of a syringe. After that, a 5 ml ethanolic solution sodium hypophosphite (84 mg, 0.8 mmol) was added to the resulting reaction mixture for

reduction of the metal salt. The reaction was then continued for 36 h at 85 °C. After the completion of the reaction, the obtained deep orange solution was cooled down to room temperature, and the solvent was removed by a rotary evaporator. The obtained product was dissolved in water and a dichloromethane mixture in a separating funnel to eliminate unreacted organic compounds. Furthermore, ~200 mg of NH₄Cl was added to the aqueous layer to extract our chloride salt precipitate of the Ru complex. Finally, the orange precipitate was filtered off and denoted as **Ru@Bpy** after drying. Analysis: C₃₆H₃₆N₆O₆Cl₂Ru (820.10) ¹H NMR (400 MHz, CD₃OD) δ 8.25 (s, 6H), 7.60 (d, J = 6.5 Hz, 6H), 7.06 (d, J = 9.2 Hz, 6H), 4.02 (s, 18H) (**Figure S1, SI**). ¹³C NMR (101 MHz, CD₃OD) δ 168.59, 160.10, 153.33, 115.04, 112.25, 57.43 (**Figure S2, SI**). ESI-MS (CH₃CN): m/z = 375.05 for (Ru(demob)₃)²⁺ ion (**Figure S3, SI**).

Synthesis of Ru@Bpy-POP: To synthesize **Ru@Bpy-POP**, carbazole (1 mmol, 167 mg) and 279 mg of the **Ru@Bpy** complex were added to 20 mL of nitromethane solvent in a 100 mL round bottom flask. Next, 1.2g of anhydrous FeCl₃ was dispersed in 20 mL of nitromethane, and the solution was added to the above-mentioned reaction mixture dropwise at N₂ atmosphere. The reaction was continued for the next 48 h at 130°C. After completing the reaction, the product was collected by washing with methanol and acetone. The greenish product was subjected to reflux in MeOH for 48 h to remove excess Fe. Finally, the **Ru@Bpy-POP** was obtained by centrifugation and kept in an oven at 100°C for drying purposes.

Electrode preparation:

For the electrocatalytic measurements, **Ru@Bpy-POP** was deposited on a nickel foam (NF) substrate. An ink of **Ru@Bpy-POP** was prepared using a 1.0 Wt% nafion solution (perfluoro sulfonated ion-exchange polymer). Next, a different amount of catalyst ink was deposited on the clean NF surface (1 × 1 cm²). The physical weight difference of NF before and after deposition indicated the amount of catalyst deposited on the NF surface. In this work, a different mass loading of **Ru@Bpy-POP** on the NF electrode was carried out, which was termed as R-1, R-4, R-5, R-7, and R-9 based on the catalyst amount 1.2, 3.8, 4.7, 7.0, and 9.4 mg, respectively, on a 1 cm² geometric surface area.

TOF calculation and mass activity determination:

For OER, turnover frequency (TOF) is defined as the moles of oxygen evolved per second (s^{-1}) per moles of total metal content. For the electrocatalyst, TOF can be calculated using the following equation.

$$TOF (s^{-1}) = \frac{j \times A}{Z \times F \times n}$$

where, j = OER current density, A = geometrical electrode surface area, $F = 96485.33289 \text{ C mol}^{-1}$, $Z = 4$ electron transfer in overall reaction, and n = mole number of transition metal. For Ru@Bpy-POP, the loading was 1.2 mg on $1 \times 1 \text{ cm}^2$ nickel foam electrode which contains 0.31 wt% Ru metal. So, the mole number of the Ru is 0.00368×10^{-3} mole. In comparison, the RuO₂ loading is 4 mg on $1 \times 1 \text{ cm}^2$ which is equivalent to 0.029×10^{-3} mole of Ru. The Current density (j) at 300 mV overpotential for **Ru@Bpy-POP** and RuO₂ are respectively 30.74 mA and 11.91 mA respectively.

Results and discussions:

In this work, we have effectively designed a redox-active Ru-integrated POP (**Ru@Bpy-POP**) through a simple template-free Friedel-Crafts (FC) alkylation polymerization between **Ru(demob)₃Cl₂** and carbazole. The roles of carbazole & **Ru(demob)₃Cl₂** could be defined as tectonic and cross-linking agents, respectively. The redox-active **Ru(demob)₃Cl₂** complex was initially synthesized through the reaction between 4,4'-Dimethoxy-2-2'-bipyridine and metal chloride precursor ($\text{RuCl}_3 \cdot x\text{H}_2\text{O}$), represented in **Figure 1**. The formation of the complex was confirmed by ¹H and ¹³C NMR spectroscopy, provided in **Figures S1** and **S2**, respectively. The chemical and physical properties of the as-synthesized **Ru@Bpy-POP** were explored through various characterization techniques.

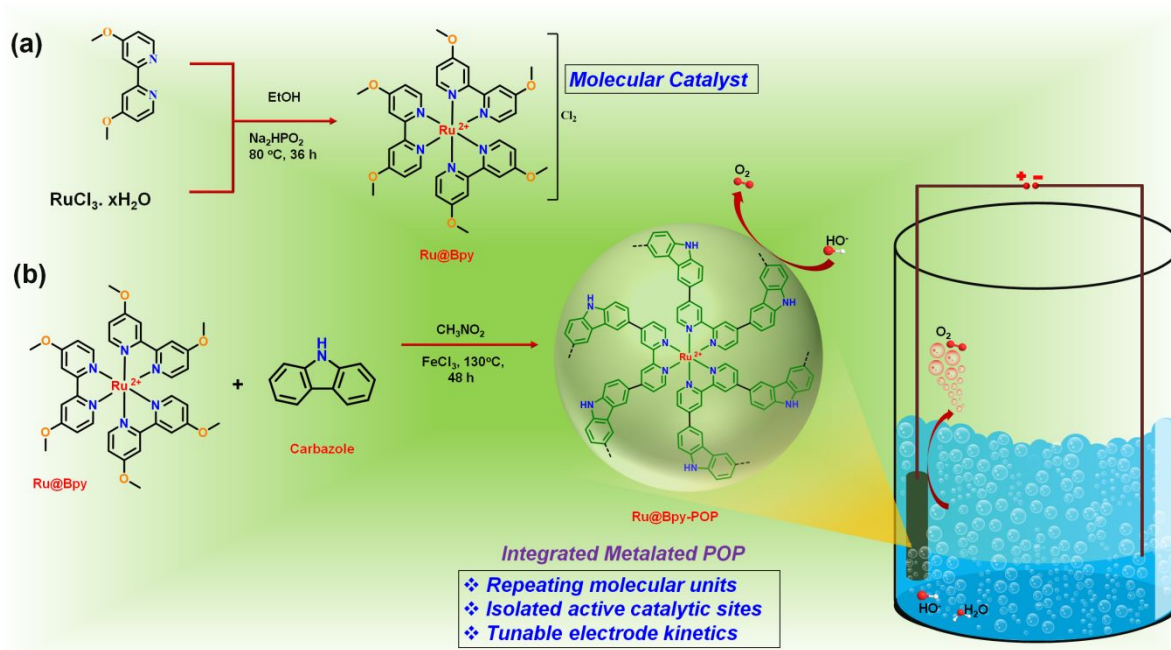


Figure 1: Schematic illustration showing the synthetic strategy of (a) as-synthesized **Ru@Bpy** and (b) **Ru@Bpy-POP** with the oxygen evolution reaction.

To reveal the thermal stability of **Ru@Bpy-POP**, thermogravimetric analysis (TGA) was carried out under an N_2 atmosphere from 25 to 700°C , as shown in **Figure S4** in the SI. The weight loss below 100°C specified the release of intercalated water and solvent molecules, which are inside the pores of the POP framework. **Figure S4** in the SI clearly indicates that our POP is stable up to 350°C . A further increase in the temperature leads to continuous weight loss due to the burning of the organic framework accompanied by C-C bond cleavage and release of small organic molecules such as CO_2 . The Ru content in **Ru@Bpy-POP** appeared to be low (0.31wt%), as revealed from inductively coupled plasma mass spectrometry (ICP-MS) analysis. Furthermore, wide-angle Powder X-ray Diffraction pattern (PXRD), Fourier Transform Infrared Spectroscopy (FT-IR), Solid-state Cross-Polarization Magic Angle Spinning Carbon-13 Nuclear Magnetic Resonance (^{13}C -CP MAS NMR), N_2 -Physisorption, Field Emission Scanning Electron Microscopy (FE-SEM), Transmission Electron Microscopy (TEM) and X-ray Photoelectron Spectroscopy (XPS) were performed on **Ru@Bpy-POP** to shed light on various inherent characteristics of the as-synthesized nanostructure to correlate with its specific activity.

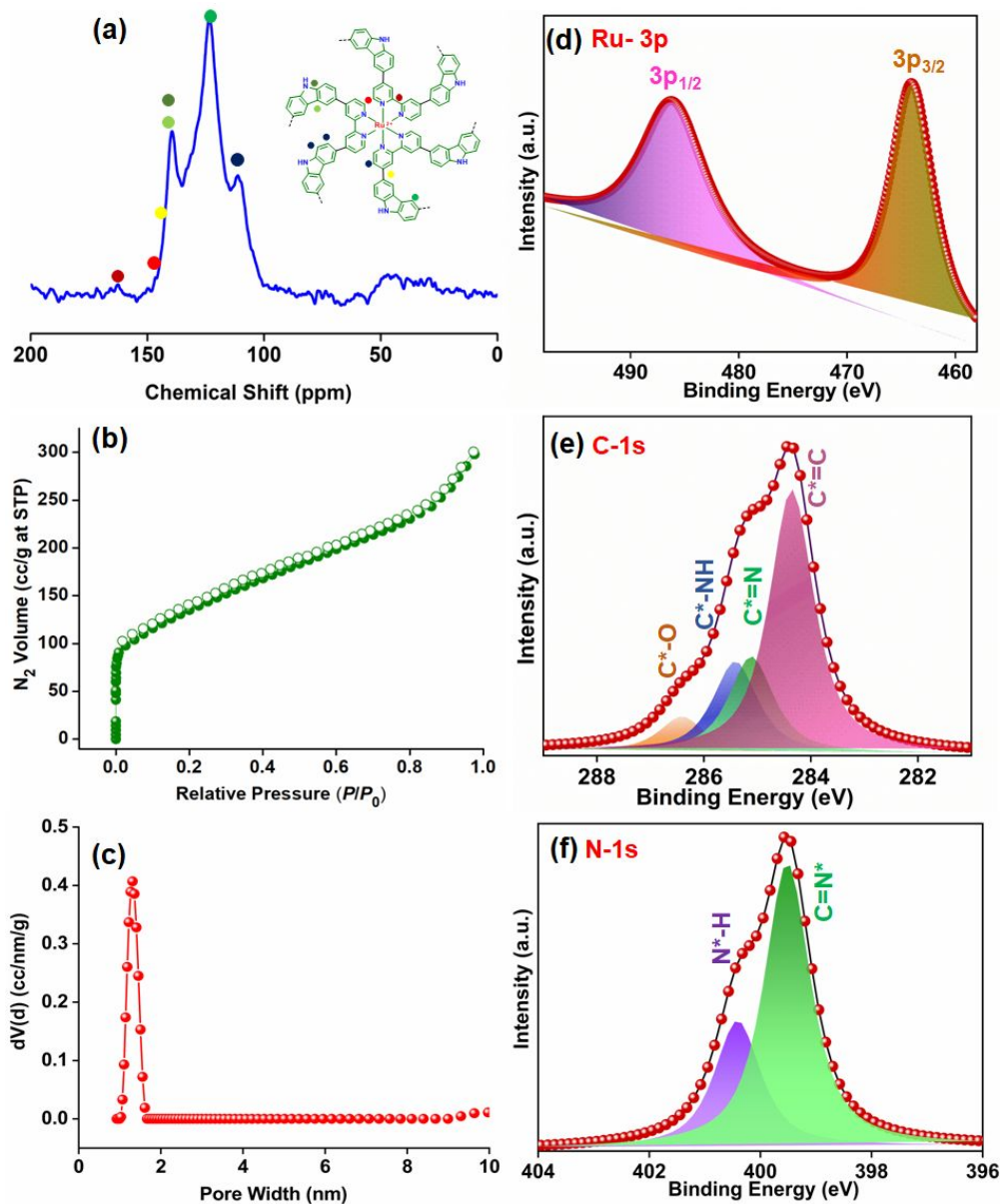


Figure 2: (a) ^{13}C -CP solid state MAS NMR spectrum, (b) N_2 -adsorption/desorption isotherms, and (c) pore-size distribution as measured by the NLDFT method of **Ru@Bpy-POP**. Core-level deconvoluted XP Spectra of (d) Ru-3p, (e) C-1s, and (f) N-1s of as-synthesized **Ru@Bpy-POP**.

Wide-angle PXRD analysis of **Ru@Bpy-POP** revealed the absence of assignable peaks in **Figure S5** in the **SI** except for a broad peak in the lower 2θ region, which clearly demonstrates an amorphous nature.¹⁹ To establish molecular connectivity and the specific chemical environment of each carbon atom present on the POP framework, ^{13}C -CP MAS NMR spectroscopy was carried out on **Ru@Bpy-POP** (**Figure 2a**). The appearance of strong resonance signals at 111 and 123 ppm, respectively, could be attributed to the unsubstituted aromatic carbon of the benzene rings on the **Ru@Bpy-POP**.²⁰ The two distinct peaks at 150

and 139 ppm, respectively, could be assigned as the main characteristic peaks related to the carbon atom attached to the nitrogen in the pyridine and carbazole ring. In addition, the carbon atom present on the pyridine and carbazole adjacent to the C=N group confirmed the peaks at 142 and 161 ppm, respectively.²¹ Hence, the structural relationship of interconnected carbon atoms on the polymeric backbone was established, which clearly illustrates the successful incorporation of both monomers into the **Ru@Bpy-POP** framework. An FT-IR spectrum elucidates the formation of the specific bond during the synthesis process with the appearance of characteristics stretching frequencies (**Figure S6** in the **SI**). The stretching frequencies at 1620 cm⁻¹ signify the presence of a C=N in the 2,2'-bipyridine heterocycle unit within the POP framework.²¹ However, the characteristic stretching frequency of N-H, an aromatic benzene ring with a carbazole moiety, appears at 3437 and 1388 cm⁻¹.²² Hence, the above-mentioned results confirmed the successful incorporation of the **Ru@Bpy** complex and carbazole monomer in the as-synthesized metallated POP skeleton. The inherent porosity of **Ru@Bpy-POP** was assessed by N₂-adsorption/desorption isotherm analysis at 77 K presented in **Figure 2b**. We have observed fully reversible isotherms accompanied by a very rapid nitrogen uptake at a very low-pressure region ($P/P_0 < 0.01$), signifying the presence of a type IV isotherm according to IUPAC classifications.²² The absence of a hysteresis loop on the N₂-adsorption/desorption isotherms confirmed no significant interaction between gas molecules and pores, resulting in identical adsorption and desorption pathways. The evaluated Brunauer-Emmett-Teller (BET) surface area of the as-synthesized **Ru@Bpy-POP** was 485 m²g⁻¹. A very narrow pore-size distribution (PSD) in the microporous region with the pore width of 1.3 nm was revealed by the Non-Local Density Functional Theory (NLDFT) method (**Figure 2c**).

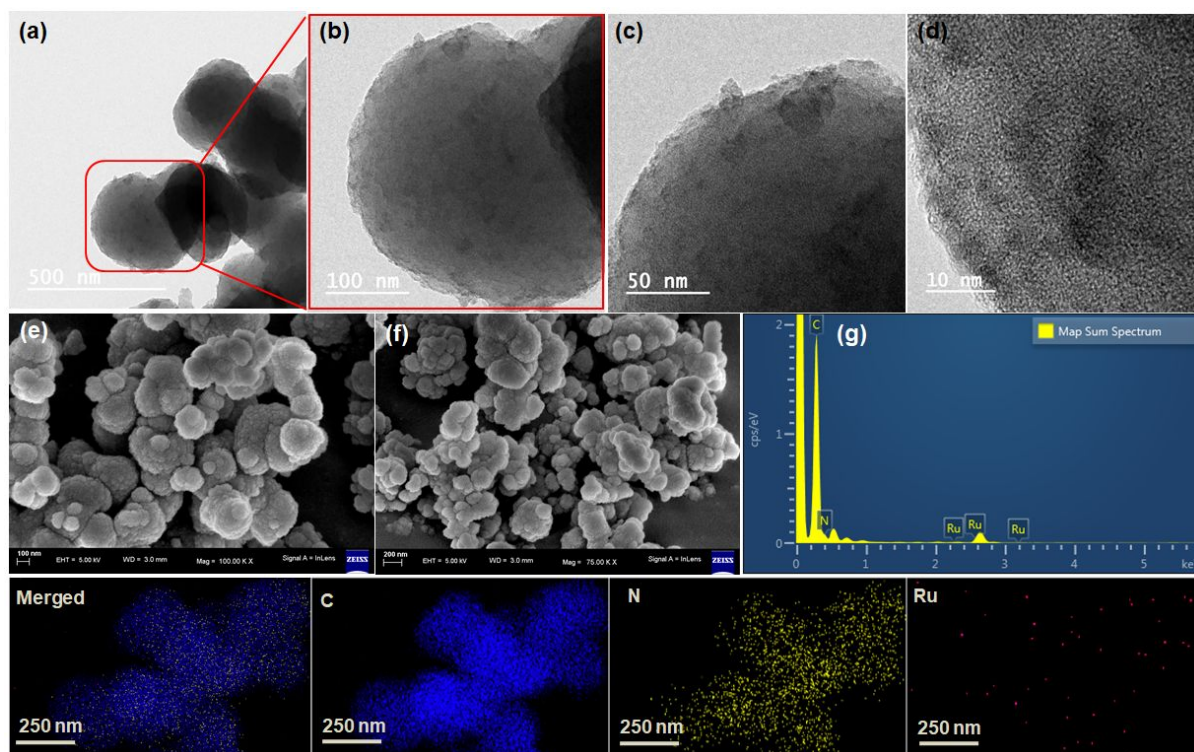


Figure 3: (a, b, c and d) TEM images, (e,f) FE-SEM images, (g) Energy-dispersive X-ray (EDX) analysis, and TEM with corresponding elemental mapping of C (blue), N (yellow), and Ru (red) of the as-synthesized **Ru@Bpy-POP**.

X-ray Photoelectron Spectroscopy (XPS) of the **Ru@Bpy-POP** was performed to reveal the elemental composition as well as the chemical and electronic state of each element present on the surface. The XPS survey spectrum presented in **Figure S9** in the SI, confirms the presence of elements C, N, and Ru, respectively. The Ru-3p core level XP spectrum exhibited two characteristic broad peaks at 463 and 485 eV, respectively, corresponding to $3p_{3/2}$ and $3p_{1/2}$, indicating the successful incorporation of the Ru complex in the POP framework (**Figure 2d**).²³ We observed four different types of peaks appearing in the C-1s XP spectrum at 284.6, 285.8, 285.4, and 286.2 eV, respectively, which could be attributed to the C=C/C-C, C=N, and C-O functional groups, respectively (**Figure 2e**). Two distinct peaks appeared at 399.5 and 400.4 eV in the high-resolution N-1s XPS, which unambiguously confirms the presence of pyridinic and pyrrolic N (**Figure 2f**).²⁴ For morphological inspection of the polymeric network, we performed a TEM analysis. The appearance of the rough surface due to the 3D growth of the metallated POP was observed (**Figure 3a**). The overlapping feature of florets over each other was clearly visible in **Figure 3b**, leading to the formation of a very dense dark area. As the concentration of metal was very low (0.31wt%), a

fluffy-shaped sphere with an almost homogeneous metal distribution was observed (**Figure 3b and 3c**).

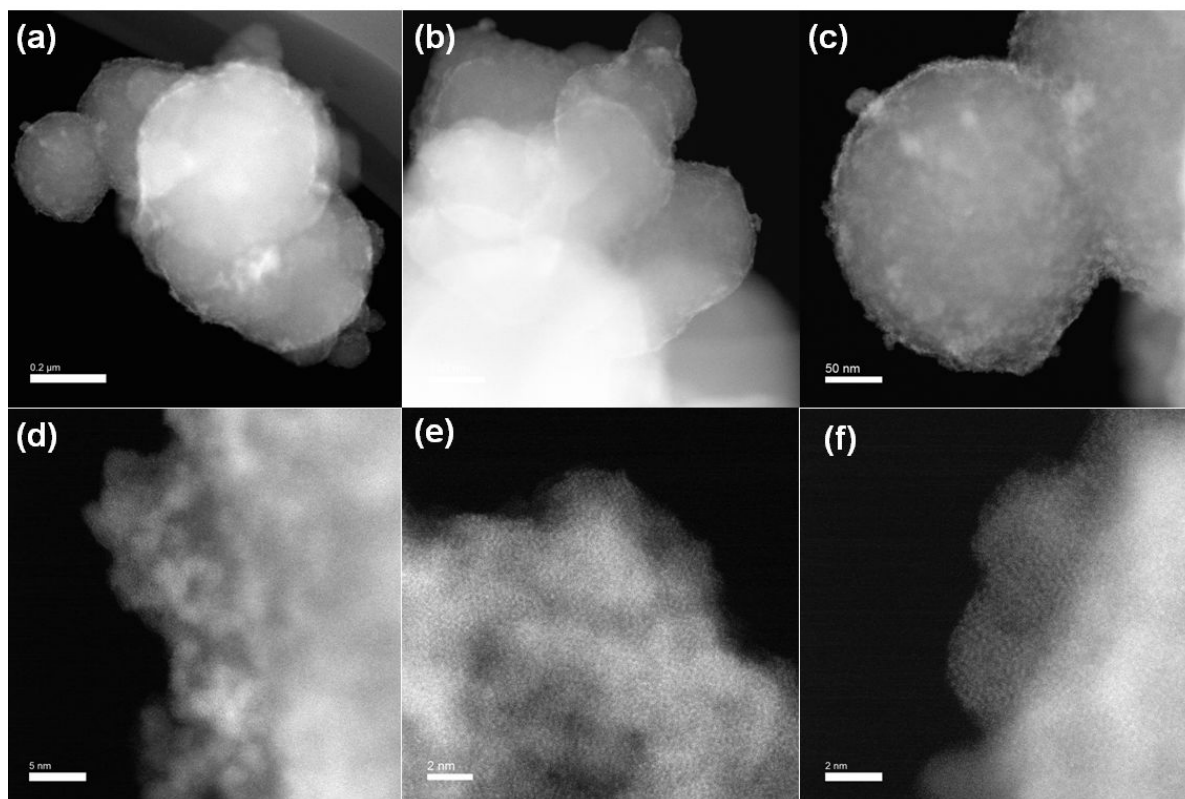


Figure 4: HAADF-STEM images of the **Ru@Bpy-POP** in (a-c) low and (d-f) high magnifications.

On closer inspection of the TEM image, the presence of a darker area symbolized the appearance of metal and polymeric networks, respectively (**Figure 3d**). Morphology of the microstructure of **Ru@Bpy-POP** was demonstrated by FE-SEM analysis, shown in **Figure 3e**. A unique feature similar to that of a cauliflower shape was observed due to the polymerization of the **Ru@Bpy** complex with a carbazole moiety. Closer inspection of the FE-SEM image of **Ru@Bpy-POP** revealed an enormous number of semi-spherical buds forming a single floret due to the specific orientation of three dimensional polymerisation during the Friedel-Crafts crosslinked polymerization process **Figure 3f**. The average floret size varies from 125-250 nm. Energy-dispersive X-ray (EDX) analysis of **Ru@Bpy-POP** clearly demonstrates the distribution of all elements, including N and Ru, over the carbonaceous framework. Transmission Electron Microscopy shows that the corresponding elemental mapping for C (blue), N (yellow), and Ru (red) are distributed in the same region in descending order accompanied by each other. The morphological evolution of the as-synthesized **Ru@Bpy-POP** along with the dispersion of Ru as active sites was also

investigated by performing high-angle annular dark-field (HAADF) scanning transmission electron microscopy (STEM) analysis in different magnifications (**Figure 4**). HAADF-STEM images of the as-prepared **Ru@Bpy-POP** sample demonstrated a nanosized sphere morphology with an average size of approximately ~250-400 nm (**Figure 4a**). All the spheres in the nanoscale dimension are strongly adhered with each other to develop a large number of irregular densely packed polymer nanoarchitectures (**Figure 4b**).²⁵ Furthermore, low magnification HAADF-STEM images show that neither the subnanometer clusters nor the nanoparticles are observed inside the void space or outside the organic polymer surfaces (**Figure 4c**). The bright white spots in the high magnification HAADF-STEM images (**Figure 4d-f**) clearly indicate that the Ru species in **Ru@Bpy-POP** are singly dispersed with a highly dense distribution.²⁶ We do agree that we can't illustrate any kind of distinguishable real morphology of Ru species as obtained from the respective HAADF-STEM images analysis (**Figure 4**). We can speculate that it may be due the ultra low loading of Ru species with much sparser dispersion inside the POP unit framework couldn't get opportunity in featuring specific morphology, is consistent with the previous finding by Ynag *et.al* in their Ru-clusters decorated core-shell metal-organic framework.²⁷ It is also important to mention that the polymer network structure has been grown with interlocked metal coordinated monomer thereby providing Ru-based isolated catalyst center in similar environment rather than that of Ru or RuO₂ nanoparticles formation (as experimentally evidenced from the PXRD & TEM images). These isolated Ru-catalyst center are tightly wrapped with dense polymer units in such a way that it got minimum exposure on the external surface to acquire some specific shape. Similar finding has been previously reported by Ma *et.al* in their Pd(II)-integrated pillarquinone-based porous polymer as heterogeneous catalyst.²⁸ Cao and co-workers have also reported Re-modified porous covalent triazine framework for highly efficient photocatalytic CO₂ reduction where Re species are dispersed but devoid of any distinct morphology of Re.²⁹ We can presume from this above observation that the single isolated Ru atoms coordinated by nitrogen species could be the active sites for the electrocatalytic OER, providing the observed promotion of the catalytic activity.

Decisive role of porous nano-structure in the electrocatalytic performance has been associated with the following reasons. Previous literature survey reported that the porous structure facilitates close contact with electrolyte thus allows more utilization of activesites.³⁰ Intrinsic nanopores have that potential to permit superior accessibility of ions electrolytes into the porous channel, thereby providing good wettability and a better interaction between

pores/electrolyte ions.³¹ The micropore (pore size < 2 nm) in such type organic polymer can create some micro cavity which promotes mass transport, easy electron diffusion, suppressed corrosion factor of the catalyst during electrocatalytic process and also enhanced charge density that strongly impacts its affinity toward OER.³²⁻³³ Based on the above previous literature reports explanations we can unambiguously conclude that the porous structure plays a crucial role in the improvement of electrocatalytic performance. Inspired with the advantageous porous nano-structural features we have explored electrocatalytic water oxidation performance of **Ru@Bpy-POP**. The electrocatalytic activity of **Ru@Bpy-POP** was evaluated using a three-electrode cell in a 1.0 M KOH electrolyte solution. **Ru@Bpy-POP** /**Nickel Foam** (NF) electrodes, a Pt wire, and Hg/HgO were provided as a working electrode, the counter electrode, and the reference electrode, respectively, in a 1 mV s⁻¹ scan rate. Commercial RuO₂ was used as a reference sample for OER and studied under the same conditions for a comparison study. Polarization curves were recorded from 1.0 to 1.7 V during the LSV study with the differently loaded **Ru@Bpy-POP** on NF as working electrodes. LSV plots recorded with the different loading of materials (R1-R6) showed that geometric current density slowly increases after the potential of 1.4 V (vs. RHE) with an onset potential of 1.42 V. A gradual increase in the current density was observed after 1.45 V and a high current density > 100 mA cm⁻² was achieved within 1.8 V vs. RHE. Notably, the R-1 electrode (loading x mg) showed an exceptionally large current density of 225 mA cm⁻² at around 1.9 V. The overpotential is a crucial factor to determine the electrocatalyst's efficiency. From the LSV curve, turnover frequency for O₂ evolution is now calculated at overpotential of 300 mV (TOF@η300) for **Ru@Bpy-POP** and RuO₂. The calculated TOF for **Ru@Bpy-POP** was 0.0216 s⁻¹ which is much higher in compared to the RuO₂ (0.001 s⁻¹). A detail calculation has now been provided in the experimental section. A comparison of the overpotentials at 10 mA cm⁻² for all the **Ru@Bpy-POP** electrodes suggests that the best activity can be achieved with R-1, i.e., only with a 1.2 mg catalyst loading. The R-1 electrode delivered a 10 mA cm⁻² current density while R-9 showed a high overpotential. R-3, R-5, and R-7 showed almost comparable overpotentials but higher than that of R-1, (**Figure 5b**) which indicates that a 1.2 mg loading can achieve a perfect monolayer of catalyst on NF support with maximum surface-exposed active sites.³⁴ The comparison of the Tafel slopes with different catalyst loading on the NF further indicated that 1.2 mg loading not only provided a perfect monolayer but also showed fast electro-kinetics with a low Tafel slope of 67 mV dec⁻¹ obtained for R-1. (**Figure 5d**) Overloading of the sample preferably blocks the active sites as

well and hinders the charge transfer in the catalyst itself. During the OER, a better surface adsorption ability of the reaction intermediates on RuO₂ makes it a reliable OER benchmark catalyst. In this regard, RuO₂ (commercial) deposited on NF would be the best reference material to compare with R-1 to judge its potential. LSV recorded under a very similar condition with RuO₂ resulted in an overpotential of 284 mV to reach a value of 10 mA cm⁻² (**Figure (5a) and (5e)**). Notably, the activity of bare NF was negligible which confirms it minimized catalytic contribution toward OER. The Tafel slope obtained for **Ru@Bpy-POP** 67mV dec⁻¹ is lower than the Tafel slope observed for the RuO₂ (346.4mV dec⁻¹) reference material (**Figure 5c**). This clearly indicates that the **Ru@Bpy-POP** exerted a faster electron movement than the commercial RuO₂.³⁵ In the OER mechanistic pathway, the active metal sites preferably play an important role in the electron transfer during the formation of reaction intermediates such as HO*, O*, and HOO* (* denotes an active site) and O-O bond formation.³⁶ The skeleton of the POP framework over the Ru leads to the reduction of aggregation and corrosion of the catalyst during electrolysis. Again, these characteristics control the active site for intermediate adsorption and reorganizes charge and spin density for the optimization of the binding energy.³⁷ The presence of POP enhances mass and electron transfer through the interconnected conjugated porous network, which is reflected in its catalytic performance.³⁸⁻⁴¹ In the POP framework, the lone pair on the pyridinic N and the delocalized π -orbitals are mainly responsible for the higher catalytic activity.⁴¹ Presumably, the Ru site acts as the active site, and the POP framework is the conductive counterpart for facile electronic movement during the OER.

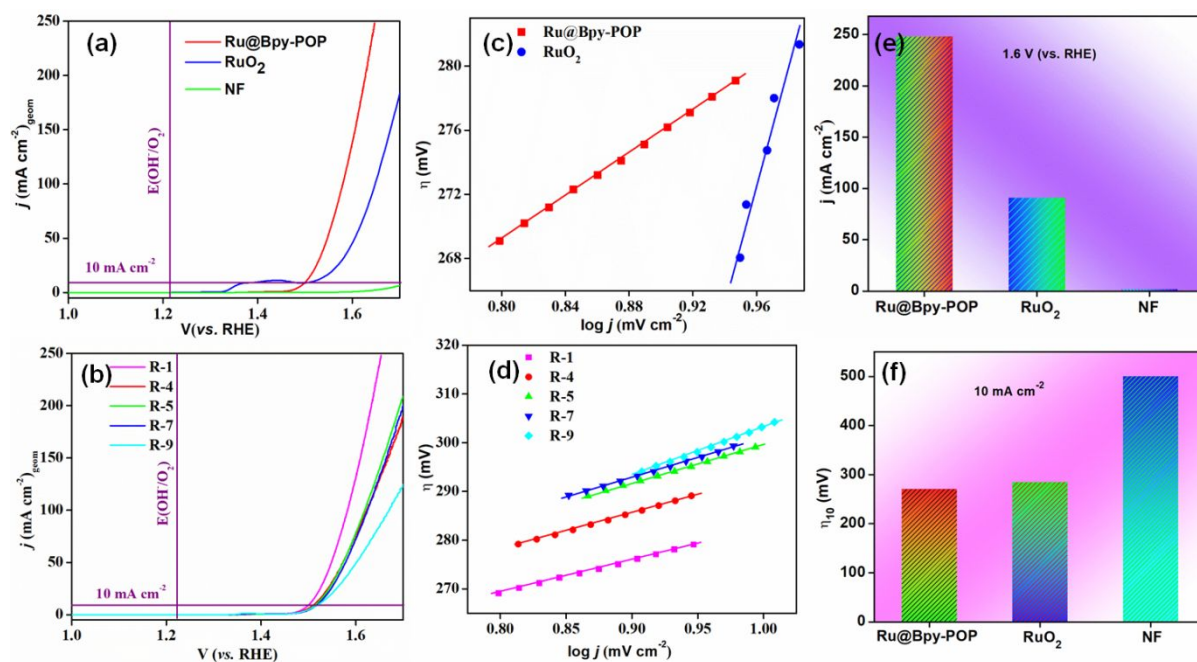


Figure 5: (a) Polarization curves obtained from the LSV of **Ru@Bpy-POP**, RuO_2 , NF using 1.0 M KOH electrolyte and (b) different amounts loaded for **Ru@Bpy-POP** on NF (R-1, R-4, R-5, R-7, and R-9). (c) Tafel slope plot of **Ru@Bpy-POP** and RuO_2 and (d) different amounts of loaded **Ru@Bpy-POP** on Nickel Foam (NF) (R-1, R-4, R-5, R-7, and R-9). (e) Current density vs. different composition (**Ru@Bpy-POP**, RuO_2 , NF) at 1.6 V vs. RHE and (f) overpotential of **Ru@Bpy-POP**, RuO_2 , NF at 10 mA cm^{-2} current density.

Electron transfer across the electrode-electrolyte also controls the kinetics of OER,³⁶ which can be understood through electrochemical impedance spectroscopic study. EIS data recorded with **Ru@Bpy-POP** was analyzed through the Nyquist plot, and showed a semi-circular behavior. Circuit fitting of the EIS data provided a low charge transfer resistance value of 1.56Ω (**Figure 6a**), which inferred better charge transfer kinetics across the electrode-electrolyte junction. The electrochemical double-layer capacitance (C_{dl}) was determined from the cyclic voltammetric scans at different scan rates in a non-faradic region (**Figure S10** in the SI). C_{dl} is directly related to the electrochemically active surface area (ECSA), and we obtain a value of 0.75 mF cm^{-2} for the **Ru@Bpy-POP** electrode, resulting in an ECSA of 0.44 (per cm^2) (**Figure 6b**).

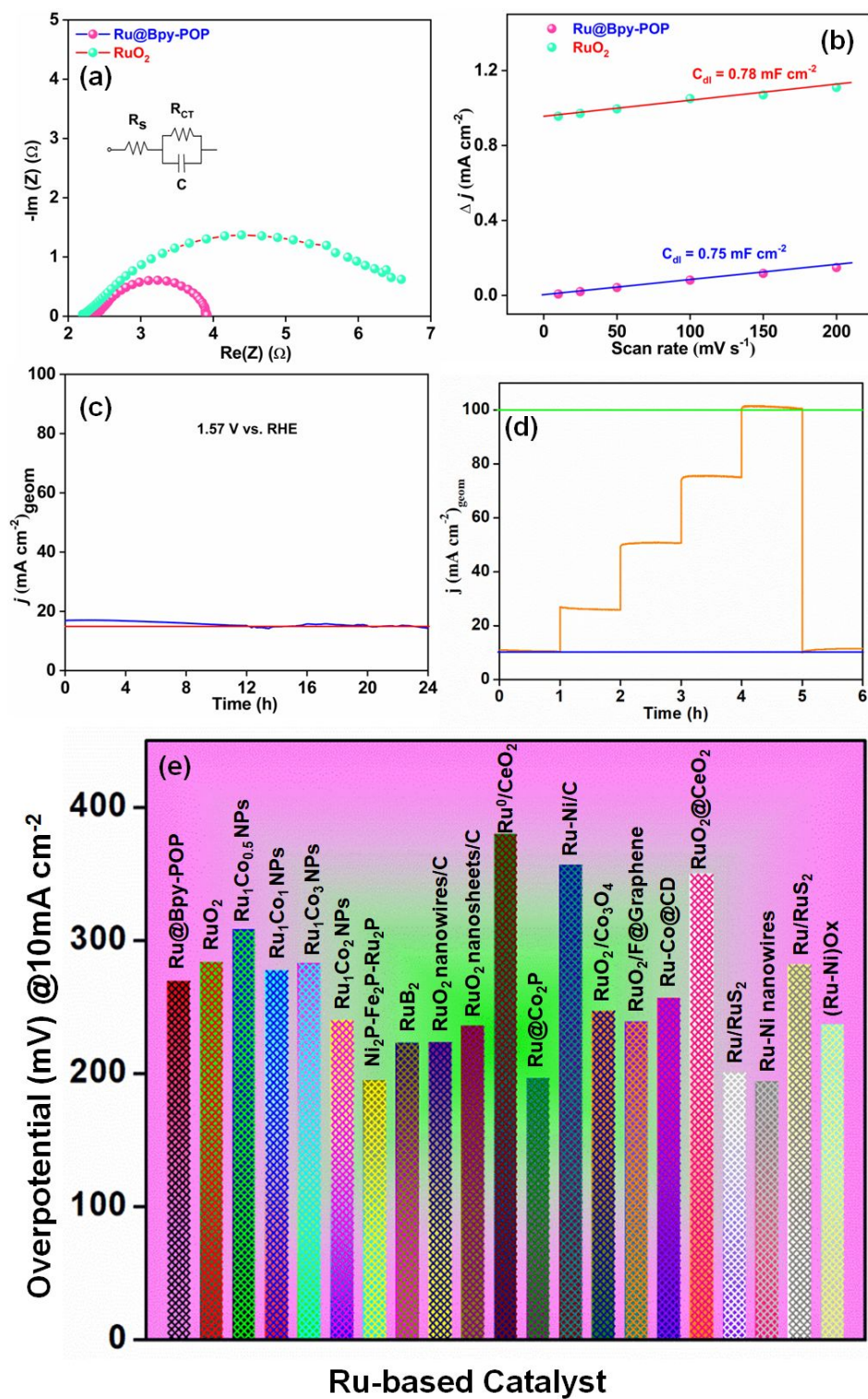


Figure 6: (a) Nyquist plot & (b) C_{dl} determined from the slopes of Δj (mA cm^{-2}) versus scan rate (mV s^{-1}) of Ru@Bpy-POP & RuO₂, (c) 24 h CA study at a potential of 1.57 V (vs. RHE), (d) Stepwise CA study for 1 h duration at 10, 25, 50, 75, and 100 mA cm^{-2} current density and (e) Overpotential of previously reported Ru-based catalyst and Ru@Bpy-POP.

The comparison of the Nyquist plot is clearly evidencing that the charge transfer resistance value of RuO₂ is much higher (4.35 Ω) than the **Ru@Bpy-POP**. This indicates that a faster charge transfer with **Ru@Bpy-POP** which provides rapid water oxidation kinetics at the electrode-electrolyte interface (**Figure 6a**). The result suggests the electronic interaction effect in the **Ru@Bpy-POP** upon the interface that improves OER kinetics. It could further be noted that the C_{dl} value for RuO₂ is 0.78 mF cm⁻² which is comparable to **Ru@Bpy-POP** (0.75 mF cm⁻²) (**Figure 6b**). ECSA (per cm²) values thereby are comparable to both the materials. The long-term stability was examined through 24 h of a chronoamperometry (CA) measurement (**Figure 6c**). Under an applied potential of 1.57 V (constant potential, vs RHE) the current density remains almost invariable over the period of 24 h. In the first 12 h of CA, a small drop (ca. 3.3 %) of *j* value was observed while it remained steady over the final 12 h of CA. Almost steady current delivery over the period of 24 h ensures the catalyst's profound durability. **Figure 6c** shows a negligible current drop in the last few hours, which indicates the stability of the electrode during the catalytic process. We also studied the durability of the electrode under a high applied potential. Notably, the **Ru@Bpy-POP** catalyst on NF can deliver very high current densities up to 25-100 mA cm⁻² for 1 h. (**Figure 6d**). A long-term durability and high density are relevant for industrial-scale water oxidation, and the sustainability performance metrics obtained in our experiments indicate the excellent robustness of the catalyst.⁴² We also performed FE-SEM analysis of the reused **Ru@Bpy-POP** catalyst to evaluate morphological changes during the OER process. We have characterized reused catalyst **Ru@Bpy-POP** after i-t test with SEM & TEM images analysis. The irregular accumulation and agglomeration during the synthesis process led to the formation of fluffy morphologies (**Figure S11** in the **SI**). On closer inspection within the range of 1 μm, we observed spherical-shaped particles stacked over each other. However, the same cauliflower-like structures of **Ru@Bpy-POP** remain unaltered in the case of reused catalyst, as shown in **Figure S11** in the **SI**. The evolution of unique semi-spherical buds of **Ru@Bpy-POP** led to the formation of floret structures (110-240 nm) due to the three-dimensional Fridel crafts polymerization between the **Ru@Bpy** complex with the carbazole moiety. For further inspection of the morphology of the reused catalyst surface, TEM analysis was performed. The overlapping feature of each floret leads to the formation of a darker area, similar to **Ru@Bpy-POP** (**Figure S12** in the **SI**). The encapsulation of the metal complex inside the porous framework probably leads to the formation of these heterogeneous features. The TEM image within the range of 20-50 nm reveals a darker area, representing

the appearance of a metal and polymeric framework as shown in **Figure S12** in the **SI**. As such, the absence of deformation of surface morphology after OER indicates the exceptional stability of our catalyst. A comparison study with various previously reported catalysts for OER is provided in **Figure 6e**. Our **Ru@Bpy-POP** electrocatalyst achieved a 10 mA cm^{-2} current density at a 270 mV overpotential compared with different reported electrocatalysts, signifying a higher electrocatalytic activity. We have also investigated the OER activity of commercially available RuO_2 by comparing it with a recently reported Ru-based catalyst. Bimetallic Ru_xCo_y NPs with different ratios of Ru and Co show good OER activity in the basic medium. Among them, Ru_1Co_2 has been evaluated as an efficient electrocatalyst that needs a lower overpotential of 240 mV with a Tafel slope is 54.4 mV dec^{-1} .⁴³ Ji-Sen Li. *et al.* recently reported an ultrathin $\text{Ni}_2\text{P-Fe}_2\text{P-Ru}_2\text{P}$ nanosheet that exhibited overall water splitting OER and HER with an overpotential 195 mV , which is significantly less for reaching a current density of 10 mA cm^{-2} .⁴⁴ Liang. *et al.* accomplished an overpotential of 224 and 236 mV for OER in an acidic medium of HClO_4 with Ru NWs and NSs supported on carbon black.⁴⁵ Akbayrak and co-workers have designed a Ru^0/CeO_2 on a glassy carbon electrode (GCE) for OER, which provides an overpotential of about 380 mV to achieve a current density of 5 mA/cm^2 .⁴⁶ Likewise, Ruthenium nanoclusters@ Co_2P , a Ru-Ni heterostructure/C, $\text{RuO}_2/\text{Co}_3\text{O}_4\text{-RuCo@NC}$, RuO_2/F doped graphene, Ru with Co doping @CD, Ru/ RuS_2 , $\text{Ni}_{\text{cluster}}\text{-Ru}$ nanowires, RuS_2 , and $(\text{Ru-Ni})\text{O}_x$ require overpotentials of about 197 , 357 , 247 , 239 , 257 , 201 , 194 , 282 and 237.2 mV , respectively.⁴⁷⁻⁵⁵ As such, our Ru-integrated POP electrocatalyst (**Ru@Bpy-POP**) exhibits a more robust framework-electrode interface with easy electron diffusion, suppressed corrosion factor of the catalyst (during electrolysis and modulation of intermediate adsorption), and enhanced charge density that strongly impacts its affinity toward OER. The mass normalized activity was obtained from the LSV of **Ru@Bpy-POP** and RuO_2 per g of material loaded in the electrode. From the mass normalized activity (**Figure S13**), it is further evident that **Ru@Bpy-POP** shows better activity compared to the RuO_2 .

To explore the electrocatalytic water oxidation reactions of **Ru@Bpy-POP**, we carried out density functional theory (DFT) calculations to calculate both its reaction energetics and electronic properties. All DFT calculations were carried out with the **FHI-AIMS** software package⁵⁸ using the Tier-1 numerical orbital basis set, which we previously showed to give reasonable agreement between accuracy and computational cost.⁵⁹⁻⁶⁰

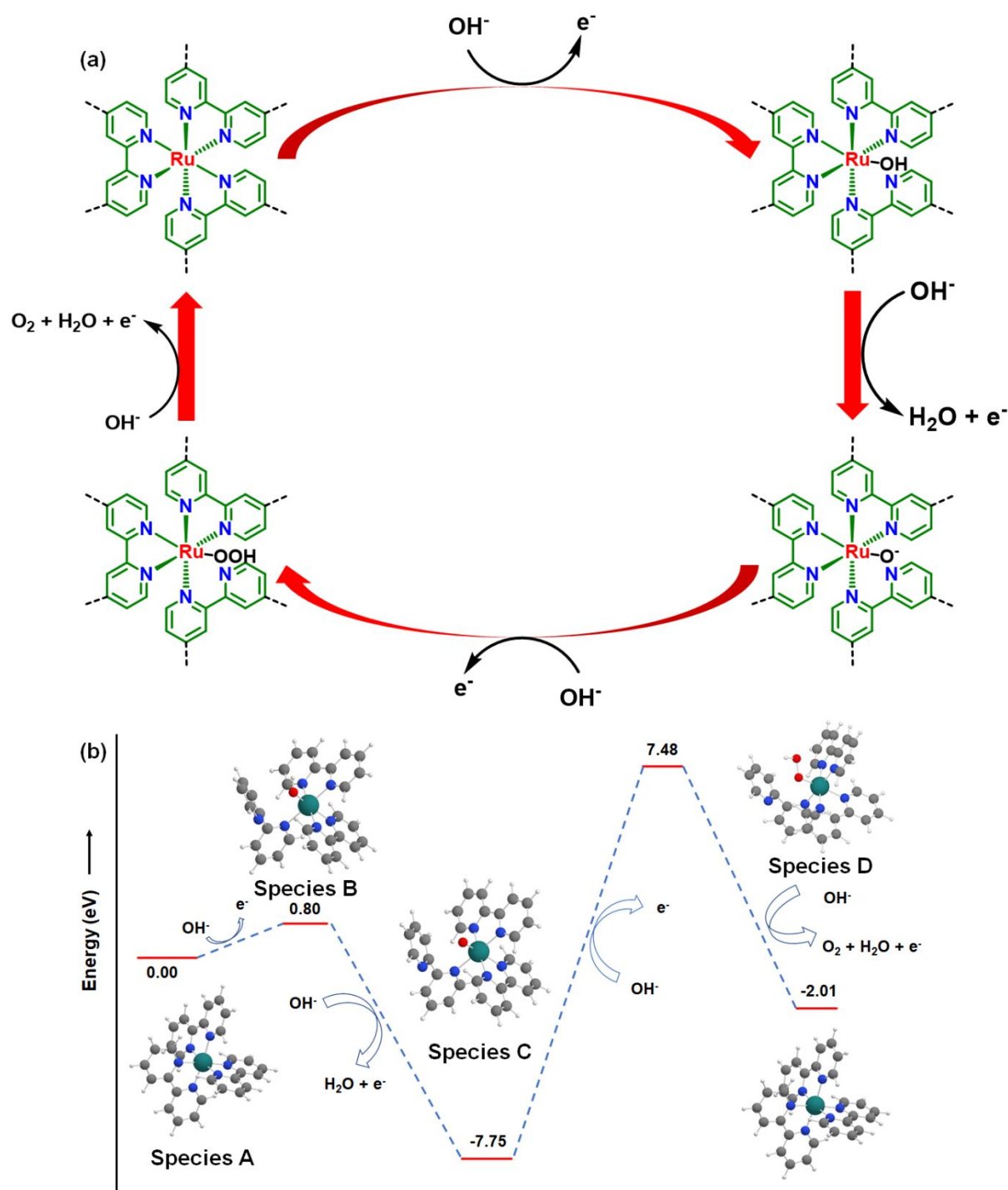


Figure 7: (a) Schematic representation of a plausible mechanistic pathway for OER of Ru@Bpy-POP in basic medium. (b) Reaction energetics for the proposed electrocatalytic water oxidation reaction of Ru@Bpy-POP at the PBE0 level of theory.

All of the molecular geometries in the proposed reaction scheme were optimized at the spin-polarized PBE level of theory⁶¹ to allow for electronic ground states having arbitrary spin multiplicities (an important effect described further below). We also explored various spin multiplicities for each geometry to ensure that we converged to the lowest-energy ground

state. After each geometry was optimized, a single-point energy calculation using the hybrid PBE0 functional⁶² was used to obtain a more accurate calculation of its reaction energetics and electronic density of states.⁶³

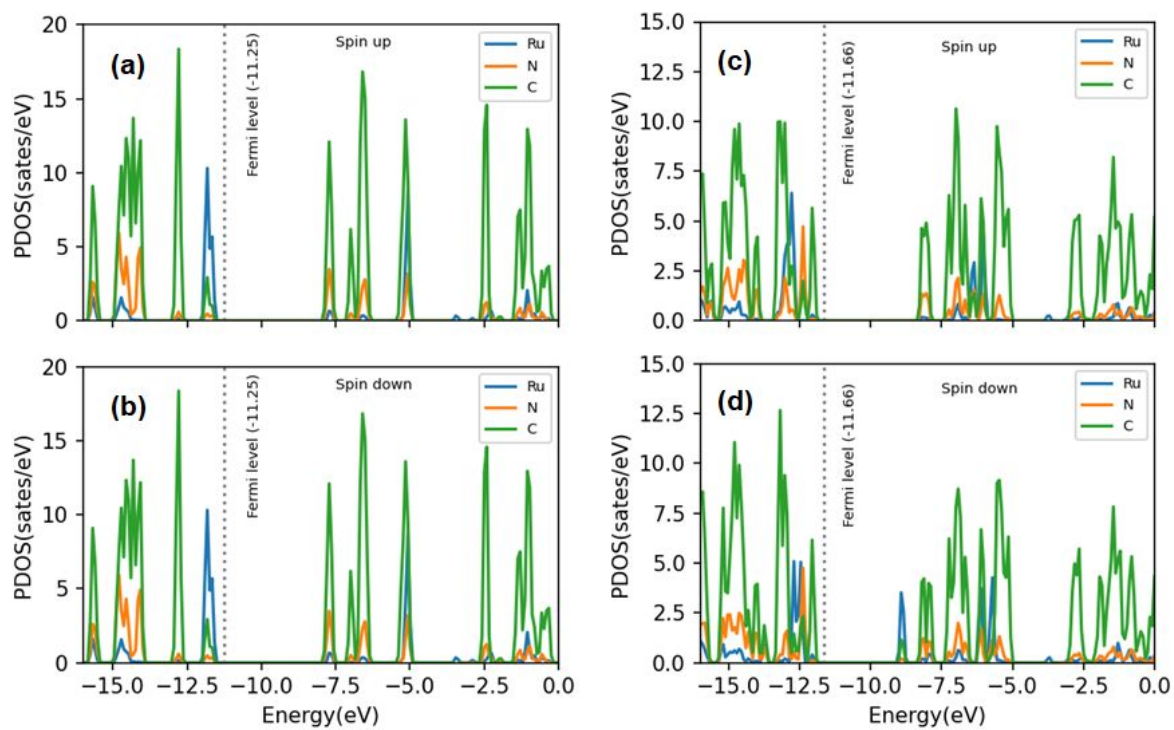


Figure 8: Partial density of states for (a,b) ‘species A’ and (c,d) ‘species B’.

Figure 7b shows the reaction energetics for the proposed electrocatalytic water oxidation reaction of **Ru@Bpy-POP** at the PBE0 level of theory. It is interesting to note that after the addition of OH^- in the first reaction step, the ground states for all the remaining structures have open-shell electronic structures with high-spin states. In other words, these high-spin states are considerably lower in energy (nearly 1.0 eV more stable) compared to their closed-shell configurations. To shed more insight into their electronic properties, we also calculated unrestricted partial density of states for each of the molecular species shown below. As mentioned previously, the first/parent molecular species has a closed-shell configuration, and the up- and down-spin density of states are identical (**Figure 8a** and **8b**). Upon addition of OH^- , a small peak corresponding to electronic states of Ru near -9.0 eV appears in **Figure 8c** and **8d**.

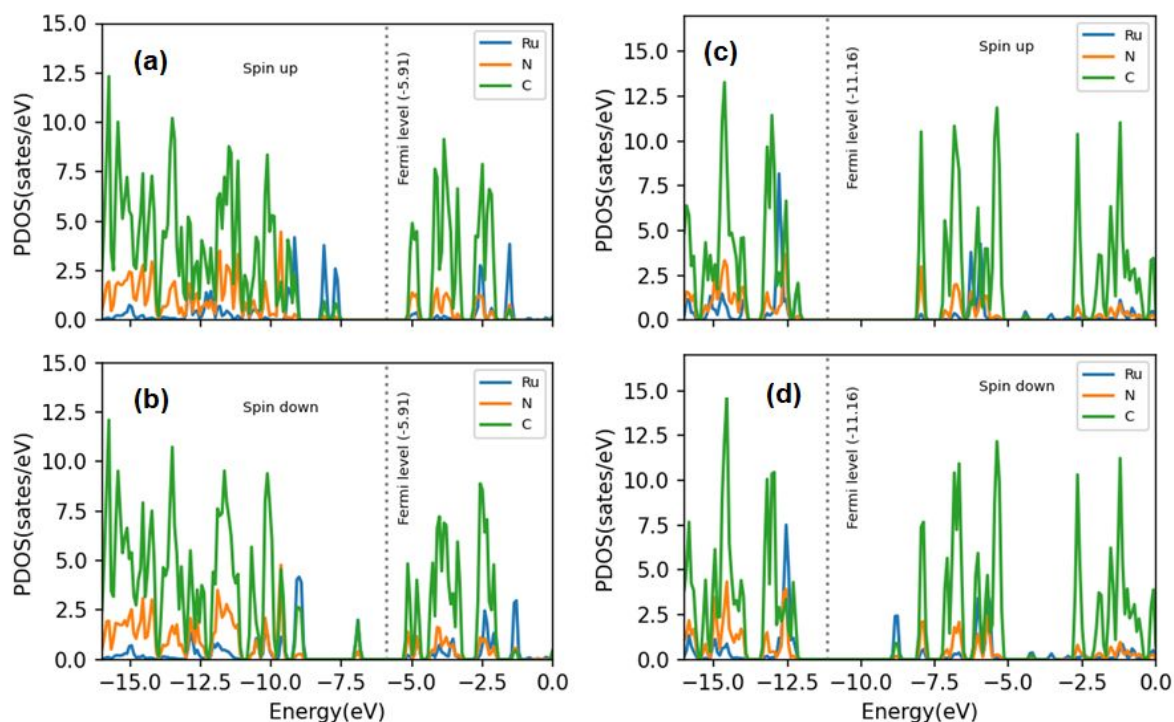


Figure 9: Partial density of states for (a,b) ‘species C’ and (c,d) ‘species D’.

When the hydrogen is abstracted from the OH ligand in the second reaction step, the Fermi level increases dramatically, such that the ruthenium orbital is now filled, and the highest occupied orbitals are primarily located on the carbon and ruthenium atoms (**Figure 9a** and **9b**). Finally, when an OH group is added in the last reaction step, the Fermi level shifts back down to -11.16 eV shown in **Figures 9c** and **9d**, resulting in the lowest unoccupied orbital corresponding to the electronic state of the ruthenium atom.

Conclusions:

In this work, we have successfully designed an atomically precise porous network modulated with a stable **Ru@Bpy-POP** electrocatalyst for OER reaction through a simple one-pot Friedel Crafts reaction between a redox-active transition metal complex $[\text{Ru}(\text{bpy})_3]^{2+}$ and a carbazole unit. The porous channel on the POP skeleton not only facilitates electron transfer during reaction but also provides stability to the catalytically active site through immobilization over the porous network. Moreover, good charge mobility over the extended polymeric network and tunable electrode kinetics accompanied by the isolated active sites play a pivotal role in the superior electrocatalytic activity of **Ru@Bpy-POP** compared to commercial RuO_2 electrocatalysts. The water oxidation ability of **Ru@Bpy-POP** with very low catalyst loading (1.2 mg) requires an overpotential of 270 mV, which is less than

expensive traditional RuO₂ (284 mV) to reach a current density of 10 mA cm⁻² with 1 M aqueous KOH solution as electrolyte. The LSV plot of OER activity exhibited a high current density of the R-1 sample (128 mA cm⁻²) in 1.6 V (vs. RHE), which is much higher than that of commercial RuO₂ (91 mA cm⁻²). The conjugated porous network of **Ru@Bpy-POP**, which contains a pyridinic N lone pair with delocalized π -orbitals, facilitates the whole electron transfer process during water oxidation and boosts its catalytic activity. The long-term stability of the catalyst was also investigated by chronoamperometry measurements for 12 h, maintaining a 10 mA cm⁻² current density, which shows negligible decay during the catalytic process. The porous network over the active Ru site reduces aggregation and corrosion, which is the main reason behind the long-term stability of the catalyst.

Conflicts of interest

There are no conflicts to declare.

Acknowledgements

B.B. and C.S. kindly acknowledge the Council of Scientific and Industrial Research (CSIR), New Delhi, for their respective junior & senior research fellowships. J.M. acknowledges the CSIR-YSA Research Grant (reference no. HRDG/YSA-19/02/21(0045)/2019) & CSIR-Focused Basic Research (FBR) Grant under the CLP theme (reference no. 34/1/TD-CLP/NCP-FBR 2020-RPPBDD-TMD-SeMI) for financial support at CSIR-IICT, Hyderabad. We also thank CSIR-IICT (Ms. No. IICT/Pubs./2022/080) for providing the required facilities to execute the research. B.C. sincerely thanks IIT-Delhi Seed grant (PLN12/04CY) and DST-INSPIRE research grant (DST/INSPIRE/04/2019/001547). The DFT calculations by S.B. and B.M.W. were supported by the U.S. Department of Energy, Office of Science, Office of Advanced Scientific Computing Research, Scientific Discovery through Advanced Computing (SciDAC) program under Award Number DE-SC0022209. We kindly acknowledge the support from Nanotechnology Platform Program of the Ministry of Education, Culture, Sports, Science and Technology (MEXT) is acknowledged for HAADF-STEM analysis.

References:

- (1) V. R. Stamenkovic, D. Strmcnik, P. P. Lopes, and N. M. Markovic, *Nat. Mater.*, 2017, **16**, 57–69.
- (2) S. H. Oh, R. Black, E. Pomerantseva, J. H. Lee, and L. F. Nazar, *Nat. Chem.*, 2012, **4**, 1004–1010.
- (3) H. Sun, Z. Yan, F. Liu, W. Xu, F. Cheng, and J. Chen, *Adv. Mater.*, 2020, **32**, 1806326.
- (4) Z. Yan, H. Sun, X. Chen, H. Liu, Y. Zhao, H. Li, W. Xie, F. Cheng and J. Chen, *Nat. Commun.* 2018, **9**, 2373.
- (5) C. C. L. McCrory, S. Jung, I. M. Ferrer, S. M. Chatman, J. C. Peters, and T. F. Jaramillo, *J. Am. Chem. Soc.*, 2015, **137**, 4347–4357.
- (6) L. Jiao, Y. Wang, H. -L. Jiang, and Q. Xu, *Adv. Mater.*, 2018, **30**, 1703663.
- (7) D. Sheberla, J. C. Bachman, J. S. Elias, C.-J. Sun, Y. Shao-Horn, and M. Dincă, *Nat. Mater.* 2017, **16**, 220–224.
- (8) E. M. Miner, T. Fukushima, D. Sheberla, L. Sun, Y. Surendranath and M. Dincă, *Nat. Commun.* 2016, **7**, 10942.
- (9) S. S. Kaye, A. Dailly, O. M. Yaghi and J. R. Long, *J. Am. Chem. Soc.*, 2007, **129**, 14176–14177.
- (10) I. J. Kang, N. A. Khan, E. Haque and S. H. Jhung, *Chem. – A Eur. J.*, 2011, **17**, 6437–6442.
- (11) S. A. Bhat, C. Das and T. K. Maji, *J. Mater. Chem. A*, 2018, **6**, 19834–19842.
- (12) P. Kaur, J. T. Hupp, and S. T. Nguyen, *ACS Catal.* 2011, **1**, 819–835.
- (13) J. Meng, Z. Xu, H. Li, D. James Young, C. Hu and Y. Yang, *ChemCatChem*, 2021, **13**, 1396–1402.
- (14) A. Vlček, *Coord. Chem. Rev.*, **2000**, 200–202, 933–978.
- (15) E. L. Sciuto, M. F. Santangelo, G. Villaggio, F. Sinatra, C. Bongiorno, G. Nicotra and S. Libertino, *Sens. Bio-Sensing Res.* 2015, **6**, 67–71.
- (16) E. Di Piazza, L. Norel, K. Costuas, A. Bourdolle, O. Maury and S. Rigaut, *J. Am. Chem. Soc.* 2011, **133**, 6174–6176.
- (17) L. Zheng, Y. Chi, Q. Shu, Y. Dong, L. Zhang and G. Chen, *J. Phys. Chem. C*, 2009, **113**, 20316–20321.
- (18) S. Zhang, W. Huang, P. Hu, C. Huang, C. Shang, C. Zhang, R. Yang and G. Cui, *J.*

- Mater. Chem. A.*, 2015, **3**, 1896–1901.
- (19) H.-K. Liu, Y.-F. Lei, P.-J. Tian, H. Wang, X. Zhao, Z.-T. Li, and D.-W. Zhang, *J. Mater. Chem. A.*, 2021, **9**, 6361–6367.
- (20) J.-H. Zhu, Q. Chen, Z.-Y. Sui, L. Pan, J. Yu and B.-H. Han, *J. Mater. Chem. A.*, 2014, **2**, 16181–16189.
- (21) Y. Zhang, L. Zhang, X. Zhang, D. Yang, C. Du, L. Wan, C. Au, J. Chen, and M. Xie, *New J. Chem.* 2020, **44**, 15202–15208.
- (22) G. Li, L. Qin, C. Yao and Y. Xu, *Sci. Rep.*, 2017, **7**, 15394.
- (23) P. H. Citrin and A. P. Ginsberg, *J. Am. Chem. Soc.* 1981, **103**, 3673–3679
- (24) N. Deka, J. Barman, J. Deka, K. Raidongia, and G. K. Dutta, *ChemElectroChem.*, 2019, **6**, 3327–3336
- (25) P. Zhail, M. Xia, Y. Wu, G. Zhang, J. Gao, B. Zhang, S. Cao, Y. Zhang, Z. Li, Z. Fan, C. Wang, X. Zhang, J. T. Miller, L. Sun and J. Hou, *Nat. Chem.*, 2021, **12**, 4587.
- (26) J.-Z. Qiu, J. Hu, J. Lan, L.-F. Wang, G. Fu, R. Xiao, B. Ge, and J. Jiang, *Chem. Mater.* 2019, **31**, 9413–9421
- (27) S. Dou, W. Zhang, Y. Yang, S. Zhou, X. Rao, P. Yan, T. T. Isimjan and X. Yang, *Int. J. Hydrog. Energy*, 2021, **46**, 7772–7781.
- (28) S. Lan, X. Yang, K. Shi, R. Fan, D. Ma, *ChemCatChem* 2019, **11**, 2864–2869.
- (29) R. Xu, X. Wang, H. Zhao, H. Lin, Y. B. Huang and R. Cao, *Catal. Sci. Technol.*, 2018, **8**, 2224–2230
- (30) M. A. Z. G. Sial, H. Lina and X. Wang, *Nanoscale*, 2018, **10**, 12975–12980
- (31) N. F. Sylla, N. M. Ndiaye, B. D. Ngom, D. Momodu, M. J. Madito, B. K. Mutuma and N. Manyala, *Sci Rep.*, 2019, **9**, 13673.
- (32) T. Sun, S. Zhang, L. Xu, D. Wang and Y. Li, *Chem. Commun.*, 2018, **54**, 12101–12104.
- (33) S. C. Shit, S. Khilari, I. Mondal, D. Pradhan, and J. Mondal, *Chem.Eur.J.*, 2017, **23**, 14827–14838.
- (34) B. Chakraborty, R. Beltrán-Suito, J. N. Hausmann, S. Garai, M. Driess, P. W. Menezes, *Adv. Energy Mater.*, 2020, **10**, 2001377.
- (35) Y. Bao, J. Dai, J. Zhao, Y. Wu, C. Li, L. Ji, X. Zhang and F. Yang, *ACS Appl. Energy Mater.* 2020, **3**, 1869–1874.
- (36) Y. Zhu, H. A. Tahini, Y. Wang, Q. Lin, Y. Liang, C. M. Doherty, Y. Liu, X. Li, J. Lu, S.

- C. Smith, C. Selomulya, X. Zhang, Z. Shao and H. Wang, *J. Mater. Chem. A*, 2019, **7**, 14222–14232.
- (37) Z. Fan, J. Jiang, L. Ai, Z. Shao and S. Liu, *ACS Appl. Mater. Interfaces* 2019, **11**, 47894–47903.
- (38) Y. Xu, S. Jin, H. Xu, A. Nagai and D. Jiang, *Chem. Soc. Rev.* 2013, **42**, 8012–8031.
- (39) X. Feng, X. Ding and D. Jiang, *Chem. Soc. Rev.* 2012, **41**, 6010–6022.
- (40) Y. Zhu, S. Wan, Y. Jin and W. Zhang, *J. Am. Chem. Soc.* 2015, **137**, 13772–13775.
- (41) S. Lu, Y. Jin, H. Gu and W. Zhang, *Sci. China Chem.* 2017, **60**, 999–1006.
- (42) Y. Gou, Q. Liu, Z. Liu, A. M. Asiri, X. Sun, and J. Hu, *Inorg. Chem. Front.* 2018, **5** (3), 665–668.
- (43) Y. Bao, J. Dai, J. Zhao, Y. Wu, C. Li, L. Ji, X. Zhang and F. Yang, *ACS Appl. Energy Mater.*, 2020, **3**, 1869–1874.
- (44) S.-H. Cai, X.-N. Chen, M.-J. Huang, J.-Y. Han, Y.-W. Zhou and J.-S. Li, *J. Mater. Chem. A*, 2022, **10**, 772.
- (45) L. Chen, Y. Li, and X. Liang, *Adv. Funct. Mater.*, 2021, **31**, 2007344.
- (46) E. Demir, S. Akbayrak, O. M. Önal and S. Özkar, *J. Colloid Interface Sci.*, 2019, **534**, 704–710.
- (47) Y. Deng, L. Yang, Y. Wang, L. Zeng, J. Yu, B. Chen, X. Zhang and W. Zhou, *Chinese Chem. Lett.*, 2021, **32**, 511–515.
- (48) J. Ding, Q. Shao, Y. Feng, and X. Huang, *Nano Energy*, 2018, **47**, 1–7.
- (49) Z. Fan, J. Jiang, L. Ai, Z. Shao and S. Liu, *ACS Appl. Mater. Interfaces*, 2019, **11**, 47894–47903.
- (50) Z. Fan, F. Liao, H. Shi, Y. Liu, M. Shao and Z. Kang, *Inorg. Chem. Front.*, 2020, **7**, 2188–2194.
- (51) T. Feng, G. Yu, S. Tao, S. Zhu, R. Ku, R. Zhang, Q. Zeng, M. Yang, Y. Chen, W. Chen, W. Chen and B. Yang, *J. Mater. Chem. A*, 2020, **8**, 9638–9645.
- (52) J. Zhu, Y. Guo, F. Liu, H. Xu, L. Gong, W. Shi, D. Chen, P. Wang, Y. Yang and C. Zhang, *Angew. Chemie.*, 2021, **133**, 12436–12442.
- (53) T. Zhu, S. Liu, B. Huang, Q. Shao, M. Wang, F. Li, X. Tan, Y. Pi, S.-C. Weng, B. Huang, Z. Hu, J. Wu, Y. Qian and X. Huang, *Energy Environ. Sci.*, 2021, **14**, 3194–3202.

- (54) Y. Zhu, H. A. Tahini, Y. Wang, Q. Lin, Y. Liang, C. M. Doherty, Y. Liu, X. Li, J. Lu, S. C. Smith, C. Selomulya, X. Zhang, Z. Shao and H. Wang, *J. Mater. Chem. A*, 2019, **7**, 14222–14232.
- (55) H. Zhang, Y. Lv, C. Chen, C. Lv, X. Wu, J. Guo and D. Jia, *Appl. Catal. B Environ.*, 2021, **298**, 120611.
- (56) D. Chen, T. Liu, P. Wang, J. Zhao, C. Zhang, R. Cheng, W. Li, P. Ji, Z. Pu and S. Mu, *ACS Energy Lett.*, 2020, **5**, 2909–2915.
- (57) S. Galani, A. Mondal, D. N. Srivastava and A. B. Panda, *Int. J. Hydrogen Energy*, 2020, **45**, 18635–18644.
- (58) V. Blum, R. Gehrke, F. Hanke, P. Havu, V. Havu, X. Ren, K. Reuter and M. Scheffler, *Comput. Phys. Commun.* 2009, **180**, 2175-2196.
- (59) S. S. R. K. C. Yamijala, Z. A. Ali and B. M. Wong, *J. Phys. Chem. C*. 2019, **123**, 25113-25120.
- (60) C. Fu, M. B. Oviedo, Y. Zhu, A. von Wald Cresce, K. Xu, G. Li, M. E. Itkis, R. C. Haddon, M. Chi, Y. Han, B. M. Wong and J. Guo, *ACS Nano*. 2018, **12**, 9775-9784.
- (61) A. D. Becke, *J. Chem. Phys.* 1992, **97**, 9173-9177.
- (62) M. Ernzerhof and G. E. Scuseria, *J. Chem. Phys.* 1999, **110**, 5029-5036.
- (63) C. Katan, P. Savel, B. M. Wong, T. Roisnel, V. Dorcet, J.-L. Fillaut and D. Jacquemin, *Phys. Chem. Chem. Phys.* 2014, **16**, 9064-9073.